Spin-piston problem for a ferromagnetic thin film: Shock waves and solitons

Mingyu Hu[1,*] Ezio Iacocca[2] and Mark A. Hoefer[1]

[1]Department of Applied Mathematics, University of Colorado, Boulder, Colorado 80309, USA

[2]Department of Physics and Energy Science, University of Colorado Colorado Springs, Colorado 80918, USA

(Received 13 January 2022; revised 21 February 2022; accepted 23 February 2022; published 17 March 2022)

The unsteady, nonlinear magnetization dynamics induced by spin injection in an easy-plane ferromagnetic channel subject to an external magnetic field are studied analytically. Leveraging a dispersive hydrodynamic description, the Landau-Lifshitz equation is recast in terms of hydrodynamic-like variables for the magnetization's perpendicular component (spin density) and azimuthal phase gradient (fluid velocity). Spin injection acts as a moving piston that generates nonlinear, dynamical spin textures in the ferromagnetic channel with downstream quiescent spin density set by the external field. In contrast to the classical problem of a piston accelerating a compressible gas, here, variable spin injection and field lead to a rich variety of nonlinear wave phenomena from oscillatory spin shocks to solitons and rarefaction (expansion) waves. A full classification of solutions is provided using nonlinear wave modulation theory by identifying two key aspects of the fluid-like dynamics: subsonic/supersonic conditions and convex/nonconvex hydrodynamic flux. Familiar waveforms from the classical piston problem such as rarefaction waves and shocks manifest in their spin-based counterparts as smooth and highly oscillatory transitions, respectively, between two distinct magnetic states. The spin shock is an example of a dispersive shock wave, which arises in many physical systems. New features without a gas dynamics counterpart include composite wave complexes with "contact" spin shocks and rarefactions. Magnetic supersonic conditions lead to two pronounced piston edge behaviors including a stationary soliton and an oscillatory wave train. These coherent wave structures have physical implications for the generation of high frequency spin waves from pulsed injection and persistent, stable stationary and/or propagating solitons in the presence of magnetic damping. The analytical results are favorably compared with numerical simulations.

DOI: 10.1103/PhysRevB.105.104419

I. INTRODUCTION

Spin transport in magnetic materials has been intensely studied, due, in part, to its potential spintronic applications in information technology. A promising means for long-distance transport of angular momentum is by way of large-amplitude, fluid-like excitations [1,2]. A useful approach to study these nonlinear spin dynamics is the hydrodynamic framework. First proposed by Halperin and Hohenberg [3] to describe spin waves in anisotropic ferro- and antiferromagnets under long-wavelength assumptions, the hydrodynamic perspective—essentially a transformation of the Landau-Lifshitz equation to a set of fluid-like variables—has since been utilized by a number of researchers to investigate a variety of novel spin textures and dynamics, sometimes referred to as superfluid spin transport [4–14]. Actually, magnetic damping implies energy dissipation, which must be compensated if sustained superfluid-like spin states are desired. An adequate compensation mechanism is the injection of spin into material boundaries via the spin-Hall effect, spin-transfer torque [6–8,10,15–17], or the quantum spin-Hall effect [18]. Recent experimental evidence of superfluid-like spin transport indicate that such dynamics are possible [15,18]. The analytical study of fluid-like spin transport in ferromagnetic materials can be conveniently formulated in terms of dispersive hydrodynamics (DH) in which large scale, nonlinear wave motion in a dispersive medium is described by conservation laws subject to dispersive corrections [19]. Such a DH formulation of magnetization dynamics was proposed in [8] as an exact transformation of the Landau-Lifshitz (LL) equation, a standard continuum, micromagnetic model of ferromagnetic materials. The DH formulation recasts the three-component magnetization vector $\mathbf{m} = (m_x, m_y, m_z)$, constrained to normalized unit length, in terms of two dependent variables: the longitudinal spin density $n = m_z$ and the fluid velocity $\mathbf{u} = -\nabla \arctan(m_y/m_x)$. The latter is proportional to the longitudinal component of the spin current. Since $m_y, m_x \to 0$ when $m_z \to \pm 1$, $\mathbf{u}$ is undefined when the magnetization is saturated in the perpendicular direction so this is referred to as the vacuum state. When the local fluid speed exceeds the critical value $u_{\rm cr} = \sqrt{(1 - n^2)/(1 + 3n^2)}$ (different from the local speed of sound due to broken Galilean invariance), the flow can be understood as supersonic [8], resulting, for example, in the generation of magnetic vortices and antivortices with vacuum states at their core [20,21]. Since the transformation is exact, the DH formulation captures all of the essential physics that are involved: exchange, anisotropy, and damping, manifesting as dispersion, nonlinearity, and viscous effects, respectively. Under conditions in which anisotropy and exchange dominate, such as when the spin density exhibits a large gradient, the spin system can develop rapidly oscillatory structures including solitons and spin shocks, also known as dispersive shock waves (DSWs), observed in the envelope of

*mingyu.hu@colorado.edu

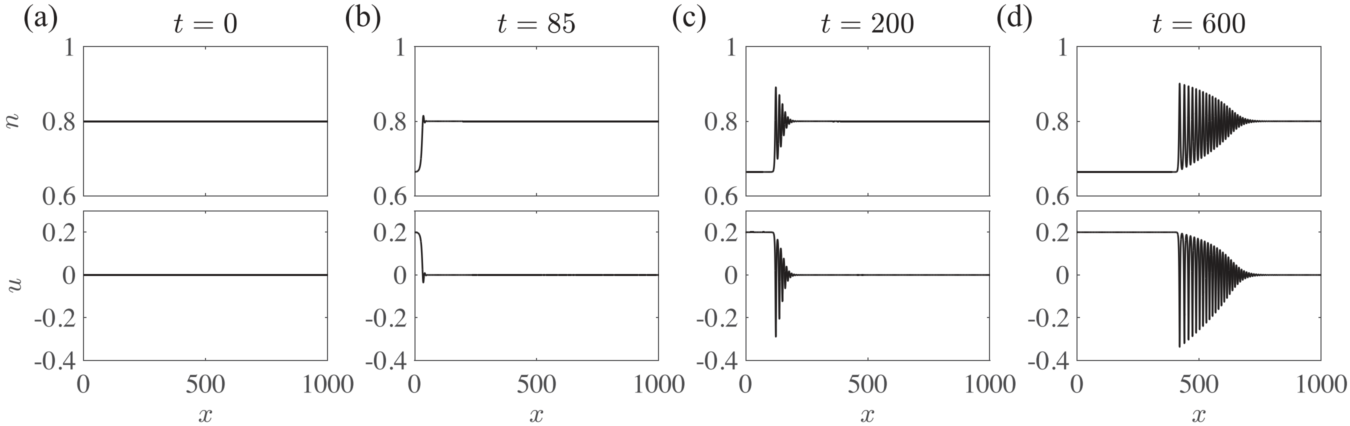

FIG. 1. Temporal development of a spin shock (DSW) solution to the piston problem in a 1D easy-plane ferromagnetic channel. (a) Initial state prior to spin piston acceleration with constant spin density $n = h_0 = 0.8$ and fluid velocity $u = 0$. (b) The piston accelerates to 99.9% of $u_0 = 0.2$ leading to a compressive wave. (c) A spin shock is under development with the constant piston velocity $u_0 = 0.2$. (d) A spin shock is fully developed.

magnetostatic spin waves in yttrium iron garnet films [22]. Such DSWs are known to occur in a variety of other DH media including Bose-Einstein condensates (BECs) [23], nonlinear spatial [24] and fiber [25] optics, and fluid dynamics [26,27]. Highly oscillatory, unsteady DSWs contrast sharply with classical shock waves that are nonlinear, dissipation-dominated, nonoscillatory and steady in viscous systems such as a compressible gas [28].

With the DH interpretation of spin dynamics in mind, we will focus on the analytical study of the canonical problem of spin injection into an easy-plane ferromagnet as a feasible mechanism to generate large-amplitude, unsteady spin textures with fluid-like features. This problem was recently considered by us in [12] by way of numerical simulations of the LL equation. We showed that the presence of a perpendicular, uniform, external magnetic field and the rapid onset of spin injection resulted in three evolutionary stages: (1) *injection rise* leading to the generation of fluid-like expansion and/or compression waves, (2) *prerelaxation* in which the dynamics are dominated by exchange and anisotropy resulting in rarefaction and shock waves, and (3) *relaxation* to steady state where damping, exchange and anisotropy result in steady, precessional dissipative exchange flows [10], also known as spin superfluids [5,6].

In the present paper, we focus on the prerelaxation stage where magnetic damping is negligible relative to exchange and anisotropy. We interpret spin injection at one material boundary as a "spin piston" whose resultant spin current is analogous to the piston velocity. To create conditions for dispersive hydrodynamics, it is crucial to implement a rapid onset of spin injection, i.e., a rapid acceleration of the spin piston until it reaches its steady velocity u_0. The piston drives fluid-like excitations into an otherwise static magnetic configuration whose spin density is determined by a perpendicular external magnetic field. Different spin injection and field strengths lead to a variety of spin rarefaction waves, spin shocks, and solitons.

The development of a spin shock generated by the spin piston is shown in Fig. 1. As demonstrated in [12], by considering the problem on short enough time scales, we can neglect magnetic damping. Therefore, in this paper, we use nonlinear wave/Whitham modulation theory [19,29–31] to analytically classify the dynamic spin textures generated by the spin piston with fixed velocity u_0 and field h_0 with negligible damping. Our primary result is the phase diagram depicting the various solution types in the injection-field (u_0-h_0) plane of Fig. 2. This diagram demonstrates the rich variety of fluid-like spin textures that can be generated in this system. Moreover, these dispersive hydrodynamic waves have physical implications for the generation of spin waves from pulsed injection and stable solitons coincident with dissipative exchange flows. In addition to the piston problem, another canonical hydrodynamic problem is the space-time evolution of an initial, sharp gradient, known as the Riemann problem [32]. We highlight the study of Ref. [33] in which the Riemann problem for polarization waves in a two-component BEC is classified. As it turns out, the governing equations studied there are equivalent to the LL equation in one spatial dimension that we study here in dispersive hydrodynamic form, neglecting dissipation due to damping. As such, we rely heavily upon the analysis carried out in [33]. Nevertheless, the piston problem studied here introduces new boundary effects that do not occur in Riemann problems such as supersonic flow conditions that generate a soliton attached to the piston or a partial DSW that emanates from it. Moreover, the spin piston problem is a physically plausible setting to generate spin shocks and other dispersive hydrodynamic spin textures in magnetic materials. Related superfluid and superfluid-like piston problems have been studied theoretically [34,35] and experimentally [36,37] in BECs and optics. While they reveal intriguing dispersive hydrodynamic features such as the generation of an oscillatory wake at the piston accompanied by vacuum points [34,37], there are a number of new effects predicted by the spin piston problem studied here. This is because the hydrodynamic flux of the spin system is *nonconvex* whereas the flux in BEC and optics is convex. Nonconvexity manifests in the spin analogues of conservation of mass and momentum with nonmonotonic hydrodynamic fluxes in the spin density and fluid velocity. In this case, the long wavelength speeds of sound coalesce. Mathematically, the long-wavelength hydrodynamic system loses

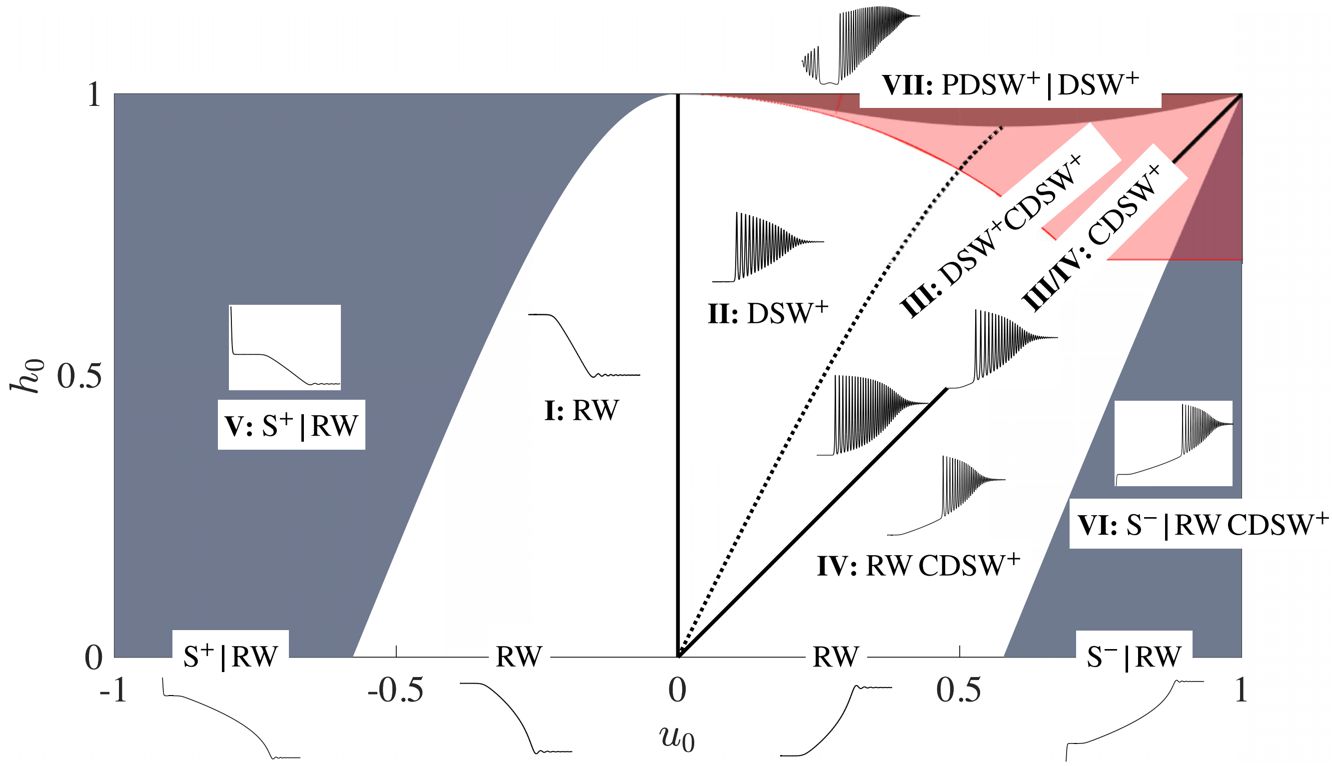

FIG. 2. Classification of spin piston dynamics in terms of the piston velocity u_0 (spin injection) and background spin density h_0 (external magnetic field). The acronyms used in the figure and throughout the text are defined in Table I. Dotted-black curve: divide between convex (left) and nonconvex (right) regimes. Solid-black lines: $r_+^L = r_+^R$ (see main text), crossover between expansion and compression. The pink-shaded region implies the existence of the vacuum state $|n| = 1$ within the oscillatory solution. The subsonic regime is identified in white. Sector I: RW; Sector II: DSW$^+$; Sector III: DSW$^+$CDSW$^+$; Boundary III/IV between sector III and IV: CDSW; Sector IV: RW CDSW$^+$. The supersonic regime is in the gray, shaded region. Sector V: S$^+$|RW, supersonic condition $v_- < v_+ < 0$; Sector VI: S$^-$|RW CDSW$^+$, supersonic condition $v_- < v_+ < 0$; Sector VII: PDSW$^+$|DSW$^+$, supersonic condition $0 < v_- < v_+$.

strict hyperbolicity and/or genuine nonlinearity. This leads to new types of dispersive hydrodynamics [38]. In addition to expanding rarefaction waves (RWs) and compressive DSWs in Figs. 1 and 2, nonconvexity results in hybrid spin textures composed of a RW and a special kind of contact spin shock or contact DSW (CDSW)—the dispersive hydrodynamic analogue of a contact discontinuity in gas dynamics—whose velocity coincides with a long wavelength magnetic speed of sound. We identify the supersonic transition at the piston as coincident with either the rapid generation of a stationary soliton or a partial DSW. Finally, sufficiently large external field and positive piston velocity result in the generation of vacuum points within the oscillatory solution. Table I lists the acronyms and symbols used throughout the main text and in Fig. 2. Table II lists the physical and mathematical properties of the all solution sectors in Fig. 2 that will be discussed in details in Secs. V–VII. Although we focus on the early, dissipationless spin dynamics, each of these distinct dispersive hydrodynamic excitations have implications for the long-time, steady-state evolution of the spin system subject to magnetic damping [12]. These implications are discussed in our concluding remarks Sec. VIII. The rest of the paper is organized as follows. Section II describes the spin piston problem setup. Section III provides a summary of the results of Whitham modulation theory from [33] so that the analysis is self-contained. Some additional analytical details

TABLE I. List of acronyms and symbols.

RW	rarefaction wave
DSW	dispersive shock wave
CDSW	contact dispersive shock wave
PDSW	partial dispersive shock wave
S	soliton
|	constant plateau separating waves
± superscripts	+: elevation soliton, −: depression soliton

TABLE II. Physical and mathematical properties of the solution sectors in the phase diagram of Fig. 2.

I: RW	subsonic, expansive, convex
II: DSW$^+$	subsonic, compressive, convex
III: DSW$^+$ CDSW$^+$	subsonic, compressive, nonconvex
IV: RW CDSW$^+$	subsonic, expansive/compressive, nonconvex
V: S$^+$|RW	supersonic, expansive, convex
VI: S$^-$|RW CDSW$^+$	supersonic, expansive/compressive, nonconvex
VII: PDSW$^+$|DSW$^+$	supersonic, compressive, convex/nonconvex

are provided in the Appendix. In Sec. V, solutions with zero applied field are presented and analyzed in both the subsonic and supersonic regimes. In Secs. VI and VII, solutions arising in the presence of a uniform perpendicular applied field are analyzed in the subsonic and supersonic regimes, respectively. Finally, we present the conclusion in Sec. VIII.

II. MODEL

Consider a one-dimensional, easy-plane ferromagnetic channel oriented in the $\hat{\mathbf{x}}$ direction with length L. Spin injection is applied to the left edge where $x = 0$. The right edge at $x = L$ corresponds to a free spin boundary. The governing equation is the nondimensional, dissipationless LL equation, given by

$$\partial_t \mathbf{m} = -\mathbf{m} \times \mathbf{h}_{\text{eff}}, \quad x \in (0, L), t > 0, \tag{1}$$

where

$$\mathbf{h}_{\text{eff}} = \partial_{xx}\mathbf{m} - m_z\hat{\mathbf{z}} + h_0\hat{\mathbf{z}}. \tag{2}$$

Here, $\mathbf{m} = \mathbf{M}/M_s = (m_x, m_y, m_z)$ is the normalized magnetization vector, and M_s is the saturation magnetization. The effective field (2) is also normalized by M_s and consists of exchange, easy-plane anisotropy, and a uniform externally applied magnetic field with constant magnitude h_0 along the perpendicular-to-plane ($\hat{\mathbf{z}}$) direction. The nondimensionalization leading to Eq. (1) is achieved by scaling time by $|\gamma|\mu_0 M_s$ and space by λ_{ex}^{-1}, where γ is the gyromagnetic ratio, μ_0 is the vacuum permeability, and λ_{ex} is the exchange length. The dissipationless LL serves as a valid model here considering the timescale within which damping is not a key factor in the development of the dynamical structures [12]. We will discuss the role of damping on longer time scales in the conclusion.

The following analysis is based on the DH formulation of Eq. (1) in terms of the hydrodynamic variables

$$\text{spin density: } n = m_z,$$
$$\text{fluid velocity: } u = -\partial_x\Phi = -\partial_x \arctan(m_y/m_x),$$

where Φ is the azimuthal phase angle. The DH formulation is given by [20]

$$\partial_t n = \partial_x[(1-n^2)u], \tag{3a}$$

$$\partial_t u = \partial_x[(1-u^2)n] - \partial_x\left(\frac{\partial_{xx}n}{1-n^2} + \frac{n(\partial_x n)^2}{(1-n^2)^2}\right), \tag{3b}$$

$$\partial_t \Phi = h_0 - (1-u^2)n + \frac{1}{\sqrt{1-n^2}}\partial_x\left(\frac{\partial_x n}{\sqrt{1-n^2}}\right), \tag{3c}$$

where (3b) follows from the negative gradient of (3c). These equations result from an exact transformation of the LL equation (1). Equation (3) is analogous to the mass, momentum, and Bernoulli equations for an inviscid, irrotational, compressible fluid. Owing to a phase singularity, the vacuum state occurs when $|n| = 1$. Equation (3) is invariant to the reflection transformation

$$h_0 \to -h_0, \quad n \to -n, \quad \Phi \to -\Phi, \quad u \to -u. \tag{4}$$

So we focus on showing results with non-negative h_0.

The boundary conditions (BCs) for Eq. (3) are

$$\partial_x n(0, t) = 0, \quad \partial_x n(L, t) = 0, \tag{5a}$$

$$u(0, t) = u_b(t), \quad u(L, t) = 0, \tag{5b}$$

where $u_b(t)$ models the time dependence of a perfect spin injection source that increases from 0 to the maximum intensity $|u_0|$ monotonically and smoothly with a rise time t_0. We adopt a hyperbolic tangent profile to model the injection rise: $u(0, t) = (u_0/2)\{\tanh[(t - t_0/2)/(t_0/10)] + 1\}$, where $t_0 = 80$ is the time that the injection magnitude reaches 99.99% of $|u_0|$. For a typical Permalloy, this hyperbolic tangent profile produces a relatively sharp change in the hydrodynamic variables—about 2 ns—when compared to the typical precessional period of spin-injected DEFs, on the order of 10–20 ns [9]. The modulationally stable region, consisting of velocities u in the interval $[-1, 1]$, corresponds to stable fluid-like configurations, so we restrict $|u_0| < 1$ [8]. The initial condition (IC) is given by

$$n(x, t = 0) = h_0, \tag{6a}$$

$$u(x, t = 0) = 0, \tag{6b}$$

with $|h_0| < 1$. Thus, the spin injection problem can be reduced to a piston problem: a piston at $x = 0$, initially with velocity $u = 0$, is accelerated to $u = u_0$, generating a flow to the right ($u_0 > 0$) or left ($u_0 < 0$) into the quiescent fluid with density $n = h_0$. In the rest of this paper, we will refer to this piston analogy for our interpretation of the spin dynamics that result from the initial-boundary value problem (3)–(6). We focus on the classification of solutions when they are fully developed such as in Fig. 1(d).

III. NONLINEAR WAVE DYNAMICS AND WHITHAM MODULATION THEORY

In this section, we provide some necessary background, primarily following [33], on Whitham modulation theory, a powerful tool for studying multiscale nonlinear wave dynamics [19,29–31]. Modulation theory results in equations that describe the slow variation of nonlinear, periodic traveling wave solutions.

A. Traveling wave solutions

Consider the traveling wave solutions of Eq. (3) in the form $n(x, t) = n(\xi)$ and $u(x, t) = u(\xi)$ with the moving coordinate $\xi = x - Vt$, where

$$V^2 = \frac{1}{2}\left(1 + \sum_{i<j}^{4} n_i n_j + \prod_{i}^{4} n_i + \sqrt{\prod_{i}^{4}(1 - n_i^2)}\right) \tag{7}$$

is the square of the wave's phase speed and n_i, $i = 1, 2, 3, 4$ are wave parameters that we will introduce shortly. The positive/negative solution for V corresponds to the right/left-going wave solutions, respectively. By insertion of $n(\xi)$, $u(\xi)$ into (3) and direct integration, the traveling wave satisfies the ordinary differential equation (ODE)

$$\left(\frac{dn}{d\xi}\right)^2 = -R(n), \tag{8}$$

where $R(n) = (n - n_1)(n - n_2)(n - n_3)(n - n_4)$ is the potential function, a quartic polynomial with zeros at n_i, $i = 1, 2, 3, 4$. The velocity field $u(\xi)$ can be obtained in terms of $n(\xi)$ and the roots n_i [33] so we focus on the modulation analysis with n. For real, ordered $n_1 \leqslant n_2 \leqslant n_3 \leqslant n_4$ in the interval $[-1, 1]$, the traveling wave solution for n either oscillates within $[n_1, n_2]$ or $[n_3, n_4]$ with wavelength given by

$$L = \frac{4K(m)}{\sqrt{(n_3 - n_1)(n_4 - n_2)}}, \tag{9}$$

where $K(m)$ is the complete elliptic integral of the first kind with m given by

$$m = \frac{(n_4 - n_3)(n_2 - n_1)}{(n_4 - n_2)(n_3 - n_1)}. \tag{10}$$

When n oscillates within $[n_1, n_2]$, the traveling wave solution is

$$n(\xi) = n_2 - \frac{(n_2 - n_1)\mathrm{cn}^2(W, m)}{1 + \frac{n_2 - n_1}{n_4 - n_2}\mathrm{sn}^2(W, m)}, \tag{11}$$

where

$$W = \sqrt{(n_3 - n_1)(n_4 - n_2)}\xi/2 \tag{12}$$

and cn, sn are Jacobi elliptic functions [39]. The velocity is given in terms of n by

$$u = -\frac{A_1 + Vn}{1 - n^2}, \tag{13}$$

where

$$A_1^2 = \frac{1}{2}\left(1 + \sum_{i<j}^{4} n_i n_j + \prod_{i}^{4} n_i \mp \prod_{i}^{4}\sqrt{1 - n_i^2}\right),$$
$$V = \sqrt{\frac{1}{2}\left(1 + \sum_{i<j}^{4} n_i n_j + \prod_{i}^{4} n_i \pm \prod_{i}^{4}\sqrt{1 - n_i^2}\right)}. \tag{14}$$

The positive square root of A_1 is taken here. The upper (lower) sign in (14) gives the fast (slow) branch of wave. V in Eq. (7) is the fast branch. We can also describe the solution in terms of an alternative set of physical wave parameters $(\bar{n}, \bar{u}, a, k)$, equivalent to n_i, corresponding to the mean spin density $\bar{n}$, mean velocity $\bar{u}$, the amplitude $a = n_2 - n_1$, and the wave number $k = 2\pi/L$.

When $n_3 \to n_2$ and $m \to 1$, the solution limits to a depression soliton

$$n = n_2 - \frac{n_2 - n_1}{\cosh^2 W + \frac{n_2 - n_1}{n_4 - n_2}\sinh^2 W}, \tag{15}$$

with background mean density $\bar{n} = n_2$. The fluid velocity in the soliton limit is

$$u = -\frac{B + c_s n}{1 - n^2}, \tag{16}$$

where

$$B = \bar{u}(\bar{n}^2 - a\bar{n} + 1) + \bar{n}\mu,$$
$$c_s = \bar{u}(2\bar{n} - a) + \mu,$$
$$\mu = \pm\sqrt{(1 - (\bar{n} - a)^2)(1 - \bar{u}^2)}, \tag{17}$$

where c_s is the soliton speed and $\bar{u}$ is the background mean velocity. The sign $+(-)$ gives the fast (slow) soliton. In terms of the roots $\{n_i\}_{i=1}^4$, c_s and $\bar{u}$ for the soliton can be obtained by taking the limit $n_3 \to n_2$ in (13) and (14).

When $n_4 \to n_3$, $m \to 0$, there are two possible limiting solutions. If $n_2 - n_1 \ll n_3 - n_1$, then the solution limits to a small-amplitude harmonic wave. If $n_2 \to n_3 = n_4$, the solution limits to a depression algebraic soliton

$$n(x, t) = n_2 - \frac{n_2 - n_1}{1 + \frac{1}{4}(n_2 - n_1)^2\xi^2}. \tag{18}$$

The background mean density for the algebraic soliton is $\bar{n} = n_2 = n_3 = n_4$. The algebraic soliton amplitude is $a = n_2 - n_1$. The background mean velocity $\bar{u}$ and algebraic soliton speed are obtained by setting $n_2 = n_3 = n_4$ in (13) and (14).

When n oscillates within $[n_3, n_4]$, the traveling wave solution is

$$n(\xi) = n_3 + \frac{(n_4 - n_3)\mathrm{cn}^2(W, m)}{1 + \frac{n_4 - n_3}{n_3 - n_1}\mathrm{sn}^2(W, m)}, \tag{19}$$

where W is given in (12). The velocity is (13) with A_1 taking the negative square root and the same V in (14).

When $n_3 \to n_2$ and $m \to 1$, the solution limits to an elevation soliton

$$n = n_3 + \frac{n_4 - n_3}{\cosh^2 W + \frac{n_4 - n_3}{n_3 - n_1}\sinh^2 W}. \tag{20}$$

The background mean density for the soliton is $\bar{n} = n_2 = n_3$. The soliton amplitude is $a = n_4 - n_3$. The background mean velocity $\bar{u}$ is obtained by taking the limit $n_3 \to n_2$ in (13) and (14). Alternatively, the fluid velocity in the soliton limit is (16) with

$$B = \bar{u}(\bar{n}^2 + a\bar{n} + 1) + \bar{n}\mu,$$
$$c_s = \bar{u}(2\bar{n} + a) + \mu,$$
$$\mu = \pm\sqrt{(1 - (\bar{n} + a)^2)(1 - \bar{u}^2)}, \tag{21}$$

where $+(-)$ gives the fast (slow) soliton.

When $n_2 \to n_1$, $m \to 0$, there are two possible limiting solutions. If $n_4 - n_3 \ll n_4 - n_1$, then the solution limits to a small-amplitude harmonic wave. If $n_3 \to n_2 = n_1$, the solution limits to an elevation algebraic soliton

$$n(x, t) = n_3 + \frac{n_4 - n_3}{1 + \frac{1}{4}(n_4 - n_3)^2\xi^2}. \tag{22}$$

The background mean density for the algebraic soliton is $\bar{n} = n_3 = n_2 = n_1$ and the soliton amplitude is $a = n_4 - n_3$. The background mean velocity $\bar{u}$ and algebraic soliton speed are obtained by setting $n_1 = n_2 = n_3$ in (13) and (14).

B. Whitham modulation equations

The modulation equations can be expressed in diagonal form by introducing new modulation variables λ_i known as Riemann invariants

$$\frac{\partial\lambda_i}{\partial t} + v_i\frac{\partial\lambda_i}{\partial x} = 0, \quad i = 1, 2, 3, 4, \tag{23}$$

where the Riemann invariants are ordered as $\lambda_1 \leqslant \lambda_2 \leqslant \lambda_3 \leqslant \lambda_4$, and the v_i are the Whitham velocities

$$v_i = \frac{1}{2}\sum_{i=1}^{4}\lambda_i - \frac{L}{2\partial L/\partial\lambda_i}, \quad i \in 1, 2, 3, 4, \tag{24}$$

where $L = \frac{4K(m)}{\sqrt{(\lambda_3-\lambda_1)(\lambda_4-\lambda_2)}}$ and $m = \frac{(\lambda_4-\lambda_3)(\lambda_2-\lambda_1)}{(\lambda_4-\lambda_2)(\lambda_3-\lambda_1)}$. The transformation between the n_i and λ_i is provided in the Appendix.

The LL-Whitham modulation equations (23) are nonconvex, namely they can lose strict hyperbolicity (two Whitham velocities coalesce) and/or they can lose genuine nonlinearity where $\frac{\partial v_i}{\partial \lambda_i} = 0$ in certain parameter regimes, resulting in a nonmonotonic dependence of the Whitham velocity on the Riemann invariant.

C. Piston sonic and convexity conditions

The modulation equations (23) exhibit two important limiting simplifications. By comparing (9) and (10), we find that the *soliton limit* ($L \to \infty$ and $m \to 1$) occurs when $\lambda_2 \to \lambda_3$ and the spin wave *harmonic limit* ($a \to 0$ and $m \to 0$) occurs when either $\lambda_1 \to \lambda_2$ or $\lambda_3 \to \lambda_4$. In these limits, two of the modulation equations coincide with the long-wave, dispersionless limit of Eqs. (3a) and (3b)

$$\partial_t \bar{n} = \partial_x[(1-\bar{n}^2)\bar{u}], \tag{25a}$$

$$\partial_t \bar{u} = \partial_x[(1-\bar{u}^2)\bar{n}]. \tag{25b}$$

The remaining two modulation equations merge and correspond to modulations of either the soliton amplitude or the spin wave wave number. The limiting velocities determine the motion of DSW edges. In the soliton limit, we have

$$s_- \equiv \lim_{\lambda_2\to\lambda_3} v_2 = \lim_{\lambda_2\to\lambda_3} v_3 = \tfrac{1}{2}(\lambda_1 + 2\lambda_3 + \lambda_4). \tag{26}$$

In one of the harmonic limits, we have

$$s_+ \equiv \lim_{\lambda_3\to\lambda_4} v_3 = \lim_{\lambda_3\to\lambda_4} v_4 = 2\lambda_4 + \frac{(\lambda_2-\lambda_1)^2}{2(\lambda_1+\lambda_2-2\lambda_4)}. \tag{27}$$

The velocities $s_- < s_+$ are the trailing and leading edges of the DSW.

The dispersionless equations (25) describe the evolution of the mean density $\bar{n}$ and mean velocity $\bar{u}$. These equations can be expressed in diagonal form

$$\frac{\partial r_\pm}{\partial t} + v_\pm \frac{\partial r_\pm}{\partial x} = 0, \quad r_\pm = \bar{u}\bar{n} \pm \sqrt{(1-\bar{u}^2)(1-\bar{n}^2)}, \tag{28}$$

where the dispersionless Whitham velocities $v_+ = \frac{1}{2}(3r_+ + r_-) = 2\bar{u}\bar{n} + \sqrt{(1-\bar{u}^2)(1-\bar{n}^2)}$, $v_- = \frac{1}{2}(r_+ + 3r_-) = 2\bar{u}\bar{n} - \sqrt{(1-\bar{u}^2)(1-\bar{n}^2)}$ are also the long-wavelength spin wave velocities. These velocities are used to identify the magnetic sonic condition [8]. The piston is subsonic if $v_- < 0 < v_+$, when

$$|\bar{u}| < u_{\rm cr}(\bar{n}) = \sqrt{\frac{1-\bar{n}^2}{1+3\bar{n}^2}}, \tag{29}$$

and supersonic if $v_- < v_+ < 0$ ($\bar{u} < -u_{\rm cr}(\bar{n})$) or $0 < v_- < v_+$ ($\bar{u} > u_{\rm cr}(\bar{n})$). Consequently, two different boundary behaviors will arise.

The dispersionless system (25) has simple wave solutions where only one of the Riemann invariants changes: (+)-waves when r_- is constant and (−)-waves when r_+ is constant. These solutions require the hyperbolic system of equations (25) to remain genuinely nonlinear [40], which holds so long as

$$\bar{u} \neq \pm\bar{n}, \quad |\bar{u}| \neq 1, \quad |\bar{n}| \neq 1. \tag{30}$$

These are the *convexity conditions*.

IV. PHASE DIAGRAM OF FIGURE 2

In this section, we provide a qualitative description of the solution types depicted in Fig. 2 as well as a quantitative description of the boundaries between the different sectors. Each distinct solution type originates from the prevailing physical and mathematical properties of the hydrodynamic equations (3) at the piston boundary: subsonic/supersonic flow, compression/expansion waves, and convexity. These properties determine the various curves partitioning the phase diagram in Fig. 2. The solution type acronyms and symbols are defined in Table I. Note that the reflection symmetry (4) implies that the phase diagram can be reflected in u_0 and h_0 to obtain the classification for $h_0 < 0$. A more detailed, quantitative description of each solution type is developed in the next three sections.

The Whitham modulation equations (23) are a set of hyperbolic equations that we will solve in order to determine the structure of solutions in the phase diagram. The oscillatory solutions we obtain here exhibit the following fundamental feature: they terminate when either the wave amplitude goes to zero (the harmonic limit) or the wavelength goes to infinity (the soliton limit). In both cases, the dispersionless equations (25) govern the mean density and velocity. A general property of hyperbolic equations such as (25) is that any dynamic front adjacent to a constant region is a simple wave [41]. Therefore, we can determine a relationship between the constant states to the left and right of the RW, DSW, CDSW, etc., by holding one dispersionless Riemann invariant constant. For the spin piston located at the left boundary, we will excite the fastest wave, a (+)-wave, in which the Riemann invariant r_- in Eq. (28) is constant across the wave

$$\begin{aligned}(+)\text{-wave:}\quad & n^L u^L - \sqrt{(1-(u^L)^2)(1-(n^L)^2)} \\ &= n^R u^R - \sqrt{(1-(u^R)^2)(1-(n^R)^2)}.\end{aligned} \tag{31}$$

The superscripts L and R denote the constant (mean) states to the left and right of the wave, respectively. In order for a (+)-wave to solve the spin piston problem, we also require the RW or DSW to propagate to the right of the boundary. Namely, we require the leftmost edge of the wave to have positive velocity

$$\text{admissibility:}\quad 0 < \begin{cases} v_+(r_-^L, r_+^L), & \text{RW}, \\ s_-(r_-^L, \lambda_2 = \lambda_3, r_+^L), & \text{DSW}. \end{cases} \tag{32}$$

It turns out that all the solutions depicted in Fig. 2 are admissible except in the supersonic sector VII.

The right state is constant, determined by the external magnetic field and free-spin boundary condition (6a), (6b)

$$n^R = h_0, \quad u^R = 0. \tag{33}$$

The constant left state is achieved after the piston velocity has saturated at $t \approx t_0$ ($u_b(t) \to u_0$), provided the admissibility condition (32) is satisfied. When the left state is subsonic, we use (31), (33), and (5b) to obtain the spin density on the left

$$\text{subsonic:}\quad n^L = h_0\sqrt{1-u_0^2} - u_0\sqrt{1-h_0^2}, \quad u^L = u_0. \tag{34}$$

The flow is subsonic so long as (29) with $\bar{u} \to u^L$ and $\bar{n} \to n^L$ is satisfied. The transition from subsonic to supersonic in the phase diagram Fig. 2 occurs when

$$|u^L| = u_{\rm cr}(n^L). \tag{35}$$

Using (34), there are multiple solutions of Eq. (35). The region of parameters corresponding to subsonic conditions at the $x = 0$ boundary is the interior of the following four curves

$$\begin{aligned} u_0 &= \pm\sqrt{\frac{2 + h_0^2 \pm h_0\sqrt{h_0^2+8}}{6}}, \\ u_0 &= \sqrt{\frac{-2 + 3h_0^2 \pm h_0\sqrt{9h_0^2-8}}{2}}, \end{aligned} \tag{36}$$

In other words, (36) are the sonic curves. The subsonic region is reflected in Fig. 2 by the unshaded and pink-shaded regions containing sectors I–IV.

Consequently, sectors V–VII are supersonic and we need an alternative way to determine n^L because $n^L \neq u_0$ at the piston boundary. Sectors V and VI are associated with the supersonic condition $v_- < v_+ < 0$ and the way to resolve this was first identified in [10] where a stationary spin soliton was introduced with its extremum in density and velocity centered at the piston boundary. Thus, only half the soliton is within the domain and it was referred to as a *contact soliton*. The soliton solutions, given by the fast branch of (15) and (20), provide for a rapid transition from supersonic conditions at the piston to subsonic conditions in the soliton far-field $(\overline{n}, \overline{u})$. In order to uniquely determine the soliton, we invoke three assumptions. First, we identify the soliton far-field with $(\overline{n}, \overline{u}) = (n^L, u^L)$. Then, for a $(+)$-wave, we can use Eqs. (31) and (33) to determine

$$n^L = -u^L\sqrt{1-h_0^2} + h_0\sqrt{1-(u^L)^2}. \tag{37}$$

Second, by equating the fluid velocity at the soliton extreme, $u(\xi = 0)$, in (16) to the fluid velocity at the piston boundary, u_0, we have

$$u_0 = -\frac{B}{1-(n^L \pm a)^2}, \tag{38}$$

where B is given in Eqs. (17) and (21), $a > 0$ is the soliton amplitude. Finally, the soliton is stationary so that $c_s = 0$ in (17) or (21), giving

$$u^L(2n^L \pm a) + \sqrt{(1-(n^L \pm a)^2)(1-(u^L)^2)} = 0. \tag{39}$$

The $+(-)$ in (38) and (39) correspond to a bright (dark) soliton. For example, in the supersonic sector V, the soliton is of elevation type so (21) applies and the $+$ sign is taken in (38) and (39). The three conditions (37), (38), and (39) uniquely determine the soliton amplitude a and its far field (n^L, u^L).

In [12], it was shown that this problem gives rise to compression or expansion waves emanating from the piston depending upon the input parameters (u_0, h_0). This is determined by whether or not the $(+)$-wave speed v_+ is increasing or decreasing from left to right during the piston acceleration period.

$$\text{compression}: \quad v_+(n^L(t), u_b(t)) > v_+(h_0, 0) \tag{40}$$

implies compression waves and expansion waves otherwise. The pure compression region is reflected in Fig. 2 by the solid-black lines $u_0 = 0$ and $u_0 = h_0$. When $0 < u_0 < h_0$, the subsonic solutions involve only DSWs. When $0 < h_0 < u_0$, the subsonic solutions involve both RWs and DSWs. When $u_0 < 0$ or $h_0 = 0$, the subsonic solutions are RWs.

When $u_0 > 0$, there is another effect at play: loss of convexity (30) when $u^L = |n^L|$. For the subsonic regime, $u^L = u_0$ and (34) implies convexity is lost when

$$\text{loss of convexity:} \quad h_0 = 2u_0\sqrt{1-u_0^2}. \tag{41}$$

This is the dotted curve in Fig. 2. To the right of this curve, the solutions exhibit hybrid waves involving CDSWs, and either DSWs (when $0 < u_0 < h_0$) or RWs (when $u_0 > h_0$).

One more feature of the solutions is depicted in Fig. 2: vacuum points. When $|n| = 1$, the velocity u is undefined and corresponds to the absence of fluid or vacuum. We find that only oscillatory solutions such as DSWs and CDSWs, i.e., $u_0 > 0$, can result in the generation of isolated points at which $|n| = 1$. The threshold for this behavior is determined by equating the extrema of the oscillation density (11) or (19) with $n = \pm 1$, namely $n_j = (-1)^j$ for some root n_j, $j \in \{1, 2, 3, 4\}$. A quantitative determination of this threshold requires the solution of the Whitham modulation equations (23), which we undertake in the next several sections. The vacuum threshold is depicted in the phase diagram Fig. 2 by a solid-red curve, above which the solutions exhibit vacuum points.

In the following sections, we solve the Whitham modulation equations to obtain the detailed structure of the shock, rarefaction, and soliton solutions.

V. ZERO APPLIED FIELD

When $h_0 = 0$, all of the dynamics are governed by the dispersionless limit (3) with additional treatment if the solution is supersonic. This case corresponds to the horizontal axis in the phase diagram Fig. 2. The $(+)$-wave for $r_+ = r_+(\xi)$ satisfies $v_+(r_-^R, r_+) = \xi = x/(t-\bar{t})$, where $\bar{t}$ is a constant time shift, $r_-^R = -1$, and $r_+^L < r_+(\xi) < r_+^R$.

A. Subsonic regime: RW

The subsonic solution when $h_0 = 0$ is a RW. The $(+)$-wave assumption leads to the background spin density on the left given by (34)

$$n^L = -u_0. \tag{42}$$

The system is always convex because $|u_0| < 1$ in (41). The admissibility condition (32) is satisfied until $v_+(r_-^L, r_+^L) = 0$, which is also the sonic condition (35) leading to $u_0 = \pm u_{\rm cr} = \pm\frac{1}{\sqrt{3}}$. Thus, for a RW solution to be admissible, the piston velocity u_0 is required to be subsonic with $u_0^2 < \frac{1}{3}$. We have additionally confirmed that there are no admissible $(-)$-wave solutions with $r_+^L = r_+^R$. The Riemann invariant configuration and an example solution is shown in Fig. 3(a). In the theoretical solution, a time delay $\bar{t} = 30$ (recall, $t_0 = 80$ is the injection rise time) is introduced to account for the piston acceleration time. This time delay is chosen to match the theoretical soliton edge location in a DSW solution as if

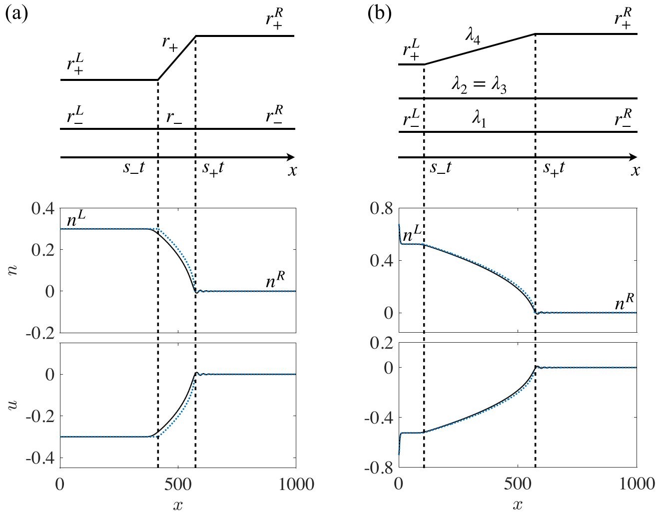

FIG. 3. Riemann invariant configurations in the upper panels corresponding to theoretical (dotted) and numerical (solid) solutions. The vertical-dashed lines correspond to $x_\pm = s_\pm(t - \bar{t})$, where $\bar{t} = 30$ is the time delay introduced to account for the piston acceleration time. (a) RW solution with $u_0 = -0.3$, satisfying the subsonic condition $|u_0| < \frac{1}{\sqrt{3}}$; (b) soliton|RW solution with $u_0 = -0.7$, satisfying the supersonic condition $\frac{1}{\sqrt{3}} < |u_0| < 1$.

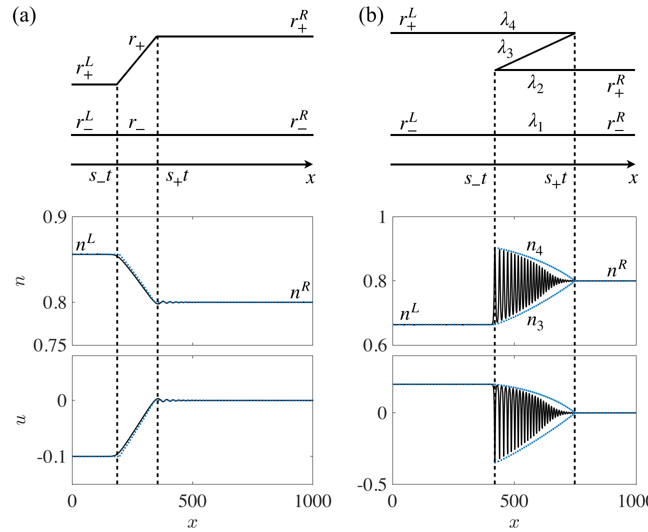

FIG. 5. Riemann invariant configurations and the corresponding theoretical (dotted) and numerical (solid) solutions. The vertical-dashed lines correspond to $x_\pm = s_\pm(t - \bar{t})$, where $\bar{t} = 30$ is the time delay introduced to account for the piston acceleration time. (a) Sector I: RW with $u_0 = -0.1$ and $h_0 = 0.8$. (b) Sector II: DSW$^+$ with $u_0 = 0.2$ and $h_0 = 0.8$, the dotted curve is the theoretical DSW envelope.

the piston was ideal with instantaneous acceleration, demonstrated later in Sec. IV B. The same choice of time delay is consistently applied to all the theoretical solutions in the following sections. Across the subsonic domain, our theoretical predictions on n^L agree excellently with simulation results, shown in Fig. 4(a).

B. Supersonic regime: S$^+$|RW

When the piston velocity is supersonic with $u_0^2 > \frac{1}{3}$, a contact soliton develops at the piston boundary, smoothly connected to a RW via an intermediate constant state. The Riemann invariant configuration of the solution is shown in the top panel of Fig. 3(b). The soliton is represented by the Riemann invariants $\lambda_2 = \lambda_3$.

This soliton is theoretically determined by (37)–(39) for a bright soliton. It is verified that when the piston is moving at the sonic speed $u_0 = u_{\mathrm{cr}} = \pm\frac{1}{\sqrt{3}}$, the soliton does not exist, i.e., $a = 0$. Therefore, the soliton at the piston boundary only emerges in the supersonic regime. A representative supersonic solution is shown in the bottom panel of Fig. 3(b) with the soliton visible close to $x = 0$, exhibiting good agreement with the numerical simulation. Across the supersonic domain, theoretical predictions of n^L and a of the soliton demonstrate excellent agreement with simulation results, shown in Fig. 4(b). Herein we have confirmed our assumptions proposed in Sec. IV on the characterization of the solitonic supersonic solutions. In addition, our analysis found that no vacuum state, where $|n| = 1$ occurs. The largest magnitude of n is reached at the peak (crest) of the elevation (depression) soliton at the piston boundary and this magnitude is always less than 1 for $\frac{1}{3} < u_0^2 < 1$.

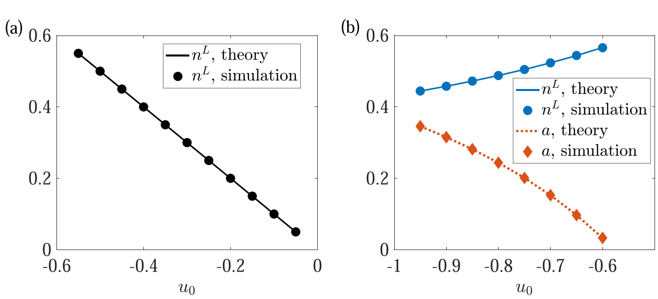

FIG. 4. Theory and simulation results of the left constant state density n^L for subsonic $|u_0| < \frac{1}{\sqrt{3}}$ (a) and supersonic $\frac{1}{\sqrt{3}} < |u_0| < 1$ (b). The soliton amplitude a is also shown in (b).

VI. NONZERO APPLIED FIELD, SUBSONIC REGIME

In this section, we present subsonic solutions with nonzero applied field. The solution map is the white region of the phase diagram Fig. 2, including sectors I–IV. We consider each sector in turn.

A. Sector I: RW

In sector I, the system satisfies the convexity condition (30) and yields simple wave solutions. Again, the solution is an expansive RW satisfying $r_- = r_-^R$, $r_+ = r_+(\xi)$, and $v_+(r_-, r_+) = \xi = x/(t - \bar{t})$. An example Riemann invariant configuration and solution in sector I is shown in Fig. 5(a). Good agreement between theory and simulation is demonstrated.

The admissibility condition (32) has been verified across sector I. The sonic condition is determined by $v_+ = 0$, yielding the boundary between sector I and V. Again, the sonic condition coincides with the admissibility threshold, indicat-

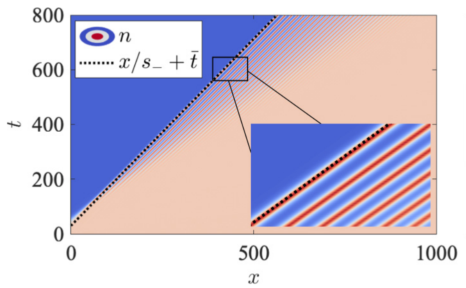

FIG. 6. Space-time contour plot of a DSW$^+$ solution in sector II with $u_0 = 0.2$, $h_0 = 0.8$. The dotted-black line is the predicted trailing edge soliton location with a time delay $\bar{t} = 30$ accounting for the piston acceleration.

ing that only subsonic solutions are admissible in sector I. On the boundary between sector I and II, which is the h_0-axis, there are no induced dynamics because $u_0 = 0$. Furthermore, no vacuum state is present in sector I since the largest magnitude of n is at the piston boundary where the piston velocity is restricted to $|u_0| < 1$.

B. Sector II: DSW$^+$

Sector II is to the left of the convexity curve (dotted-black curve) in the phase diagram Fig. 2, so the system is convex, yielding simple wave solutions. Furthermore, $v_+(r_-^R, r_+^L) > v_+(r_-^R, r_+^R)$ leads to compressive DSW solutions that satisfy $\lambda_3 = \lambda_3(\xi)$, $v_3(r_-^R, r_+^R, \lambda_3, r_+^L) = \xi = x/(t - \bar{t})$. The DSW solutions satisfy the admissibility condition (32). An example Riemann invariant configuration and solution in sector II is shown in Fig. 5(b). Near the DSW's harmonic edge, the numerical simulation and the predicted envelope amplitude deviate somewhat. This is a common feature of the asymptotic (large t) behavior of DSWs [19]. Figure 6 shows that the theoretically predicted trajectory of the DSW's soliton edge aligns with the simulation result by incorporating a time delay $\bar{t} = 30$ to account for the piston acceleration period. The DSW solution exhibits vacuum in the pink-shaded region in the phase diagram Fig. 2. The vacuum state is first reached when the maximum of the trailing edge soliton density $n = n_4$ reaches 1. We evaluate n_4 in the soliton limit, which is a function of the Riemann invariants, to determine this threshold (see Appendix). As time progresses, the vacuum point moves inside the oscillatory structure [19]. Example DSWs with vacuum will be shown in Fig. 7. We point out that the vacuum threshold determination is the same across all subsonic sectors whose solution contains a DSW structure, despite the convexity of the system.

C. Sector III: DSW$^+$CDSW$^+$

Sector III is to the right of the convexity curve (dotted-black curve) in the phase diagram Fig. 2, so the solution breaks the convexity condition (30), manifested as the coalescence of two Riemann invariants $\lambda_3 = \lambda_4$ and Whitham velocities $v_3 = v_4$. The Riemann invariant configuration and an example solution are shown in Fig. 8(a), satisfying $r_- = r_-^R$, $\lambda_3 = \lambda_3(\xi)$, and $v_3(r_-^R, r_+^R, \lambda_3, r_+^L) = \xi = x/(t - \bar{t})$. The spin injection u_0 satisfies (40), leading to a compressive

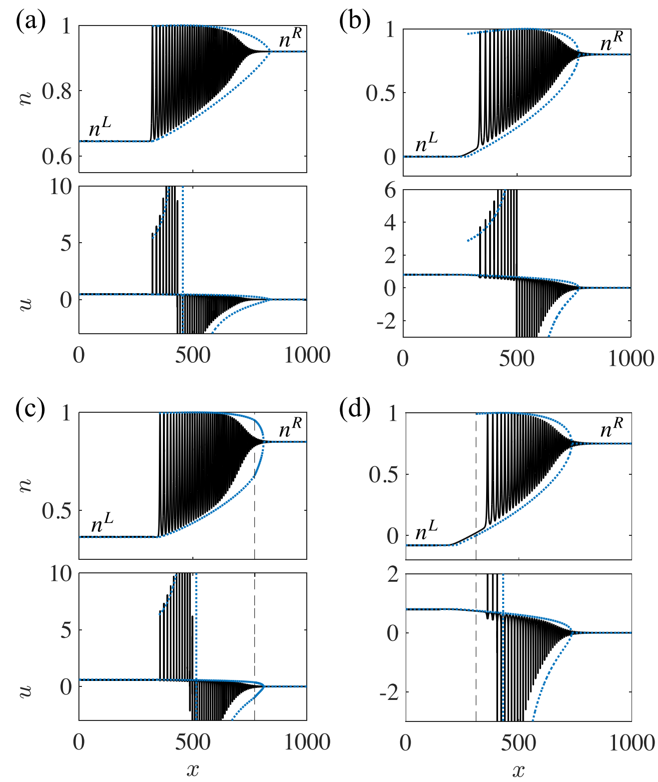

FIG. 7. Example solutions with vacuum states when $h_0 \neq 0$. (a) Sector II: DSW$^+$ with $u_0 = 0.45$ and $h_0 = 0.92$; (b) Border of sectors II and III: CDSW$^+$ with $u_0 = 0.8$ and $h_0 = 0.8$; (c) Sector III: DSW$^+$CDSW$^+$ with $u_0 = 0.6$ and $h_0 = 0.85$; (d) Sector IV: RW CDSW$^+$ with $u_0 = 0.8$ and $h_0 = 0.75$. The dotted curves are the predicted envelopes of the DSW structure. In (d), the dotted curve includes the predicted dispersionless RW portion in the solution. The vertical-dashed lines separate different components in composite modulation solutions. The modulation solutions includes the time delay $\bar{t} = 30$ to account for the piston acceleration time.

DSW$^+$CDSW$^+$ composite wave where $r_+^L > r_+^R$ gives the DSW portion and the coalescence of Riemann invariants $\lambda_3 = \lambda_4$ gives the CDSW portion.

A CDSW is a degenerate DSW solution whose soliton limit is an algebraically decaying soliton where three Riemann invariants, λ_2, λ_3, and λ_4, coincide. The algebraic soliton travels at the speed of a dispersionless (long-wave) characteristic velocity, mimicking a contact discontinuity in viscous hydrodynamics. It is observed numerically that CDSWs generally require a longer time than DSWs to develop. Therefore, a larger discrepancy between the simulated CDSW portion and the analytical wave envelope is observed compared to the DSW portion. The admissibility of the composite wave solution in sector III, $0 < s_-^{(1)} < s_-^{(2)} < s_+$, has been confirmed. The region where a vacuum state is present in the solution is shaded in pink in Fig. 2 and a typical solution is shown in Fig. 7(c).

D. Sector IV: RW CDSW$^+$

Before moving on to sector IV, we discuss the solution on the boundary between sector III and IV, where $r_+^L = r_+^R$

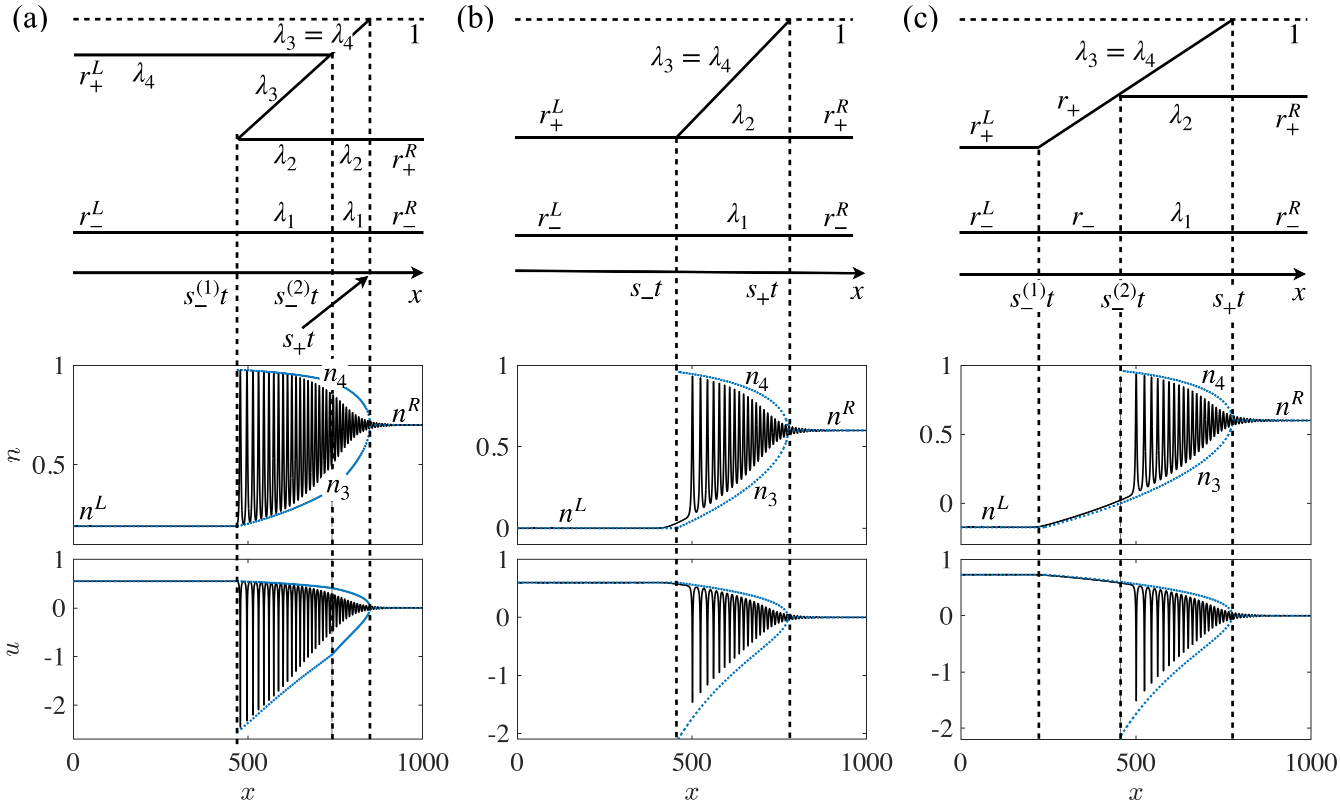

FIG. 8. Riemann invariant configurations and example solutions when $h_0 \neq 0$ for (a) Sector III: DSW$^+$CDSW$^+$ with $u_0 = 0.55$ and $h_0 = 0.7$; (b) Boundary of sectors III and IV: CDSW$^+$ with $u_0 = 0.6$ and $h_0 = 0.6$. (c) Sector IV: RW CDSW$^+$ with $u_0 = 0.73$ and $h_0 = 0.6$; The vertical-dashed lines separate different components of the composite wave solutions based on predicted edge velocities. The dotted curves are the predicted envelopes of the DSW structure in the solution. In (b), the dotted curve also predicts the dispersionless RW portion of the solution. All modulation solutions include the time delay $\bar{t} = 30$ to account for the piston acceleration time.

as shown in the Riemann invariant configuration in Fig. 8(b). The system is nonconvex and the solution is a single CDSW$^+$ because $\lambda_3 = \lambda_4$ across the shock. Sector IV is to the right of the convexity threshold [dotted-black curve, Eq. (41)] in Fig. 2, so the system is nonconvex. During piston acceleration, compressive dynamics are induced, then followed by expansive dynamics. Thus, the solution is a RW CDSW$^+$ composite wave that satisfies $r_- = r_-^R$, $v_3(r_-^R, r_+^R, \lambda_3, \lambda_3) = \xi = x/(t - \bar{t})$, and $\lambda_4 = \lambda_3$.

The Riemann invariant configuration and an example solution are shown in Fig. 8(c). The admissibility (32) of the solutions have been verified in the sector with the threshold $s_-^{(1)} = 0$ coinciding with the sonic condition $v_+ = 0$ and Eq. (35). The vacuum region, shaded in pink in Fig. 2, is determined by evaluating the wave envelope n_4 in the algebraic soliton limit. The onset of vacuum is found to be independent of u_0 in this case and happens at $h_0 = 1/\sqrt{2}$. Representative solutions containing a vacuum point are shown in Figs. 7(c) and 7(d).

In the example solutions shown in Figs. 8(b) and 8(c), we observe that there is a smooth tail at the algebraic soliton limit of the CDSW when it connects to the dispersionless portion of the solution. This phenomenon is most evidently shown in Fig. 8(b) with a single CDSW. This behavior does not occur in DSWs where the exponential soliton edge terminates directly at the dispersionless edge state [see the bottom panels of Figs. 5(b) and 8(a)]. This phenomenon serves as a distinguishing feature to identify the soliton edge of a CDSW.

VII. NONZERO APPLIED FIELD, SUPERSONIC REGIME

Sectors V and VI satisfy the supersonic condition (35) in which $v_- < v_+ < 0$ and a contact soliton is developed at the piston boundary. Sector VII also satisfies the supersonic condition where $0 < v_- < v_+$ and a PDSW emanates from the piston boundary.

A. Sector V: S$^+$|RW

The contact soliton is uniquely determined by (37)–(39). With the determined soliton far-field $(n^L, u^L) = (\bar{n}, \bar{u})$, the modulation solution is an expansive RW, satisfying (31) and $r_+ = r_+(\xi)$ where $v_+(r_-, r_+) = \xi = x/(t - \bar{t})$. The admissibility condition (32) is satisfied. Similar to the zero field supersonic solution, no vacuum point is attained. A representative solution is shown in Fig. 9(a) with quantitative agreement between the theoretical prediction and the numerical simulation.

B. Sector VI: S$^-$|RW CDSW$^+$

The depression contact soliton is uniquely determined by (37)–(39) with far-field $(n^L, u^L) = (\bar{n}, \bar{u})$ breaking the

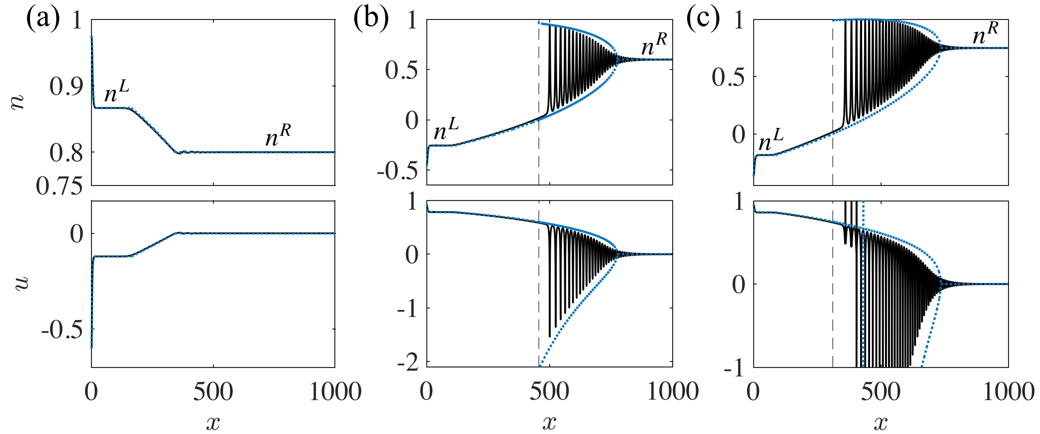

FIG. 9. Supersonic solutions when $h_0 \neq 0$. (a) Sector V: $S^+|RW$ with $u_0 = -0.6$ and $h_0 = 0.8$; (b) Sector VI: $S^-|RW\,CDSW^+$ with $u_0 = 0.92$ and $h_0 = 0.6$; (c) Sector VI: $S^-|RW\,CDSW^+$ with a vacuum point, $u_0 = 0.96$ and $h_0 = 0.75$. The dotted curves trace the predicted piston edge soliton, the dispersionless portion of the solution, and the envelope of the DSW-type portion of the solution. The vertical-dashed lines divide the different components in a composite wave based on the predicted edge velocities. The time delay $\bar{t} = 30$ is used in theoretical plotting to account for the piston acceleration time.

convexity condition (30), leading to a RW CDSW$^+$ composite wave satisfying $r_- = r_-^R$, $v_3 = (r_-^R, r_+^R, \lambda_3, \lambda_3) = \xi = x/(t - \bar{t})$, and $\lambda_4 = \lambda_3$. A representative solution is shown in Fig. 9(b). Same as in sector IV, the onset of vacuum, when the algebraic soliton of the CDSW portion reaches 1, is independent of u_0 and happens at $h_0 = 1/\sqrt{2}$. The pink-shaded region in Fig. 2 indicates a vacuum state is present in the solution. A vacuum solution from this sector is shown in Fig. 9(c).

C. Sector VII: PDSW$^+$|DSW$^+$

The supersonic condition $|u_0| > u_{\rm cr}(n^L)$ in sector VII is $0 < v_- < v_+$. This positive velocity configuration is different from all other supersonic sectors with negative dispersionless velocities. It gives rise to a PDSW [42] at the piston edge. For this sector, we have not been able to develop quantitative, theoretical descriptions for the composite waves using modulation theory, so we focus on the qualitative identification of the solution features with the support of simulations. As we observed numerically [see Fig. 10(a) for example], the PDSW is led by a soliton at its right edge and terminates on the left at the piston boundary without reaching the small amplitude limit. The intermediate state connecting the PDSW and a DSW-type wave demonstrates slow oscillations that possibly is not a constant plateau and requires additional analysis. Without the PDSW far-field determined, we are unable to determine the modulation solution. Note that a vacuum point is present inside the solution, consistent with our prediction in Fig. 2.

We have numerically confirmed that along the sonic curve bounding the subsonic sector II, where the system remains convex, there is no PDSW emerging from the piston boundary. However, within the nonconvex subsonic sector III when near the sonic curve at the sector VII boundary, we numerically observed that a PDSW develops at the piston boundary as shown in Fig. 10(b). Consequently, the predicted sonic boundary between sectors III and VII does not precisely explain this phase change. We have not been able to quantitatively identify the threshold for the occurrence of this phase transition using modulation theory. However, all simulations that we have performed in sector VII exhibit this PDSW structure.

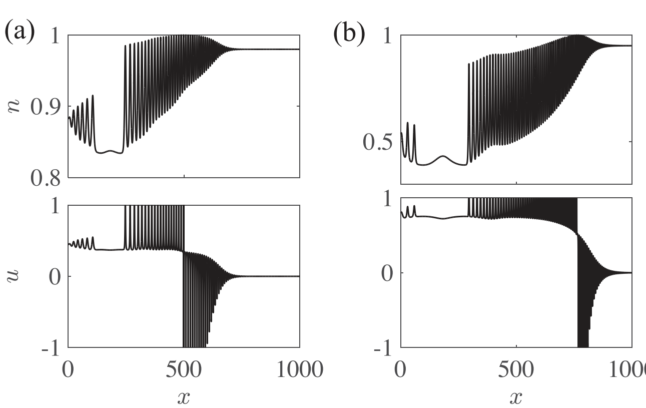

FIG. 10. (a) PDSW|DSW$^+$ solution in sector VII with $u_0 = 0.45$ and $h_0 = 0.98$. (b) Supercritical solution in sector III with $u_0 = 0.8$ and $h_0 = 0.95$.

VIII. CONCLUSIONS

Using the dispersive hydrodynamic framework, we have analytically classified the piston-like dynamics of a dissipationless easy-plane ferromagnetic channel subject to spin injection at one channel boundary. This framework enables the analytical description of noncollinear magnetic textures beyond the small-amplitude, weakly nonlinear regime.

Two properties of the system are fundamental to our analysis. First, the piston analogy naturally leads to the investigation of magnetic sub- to supersonic conditions, corresponding to distinct piston boundary behavior: either a constant hydrodynamic flow in the subsonic case, or a soliton or a non-stationary partial DSW (PDSW), both in the supersonic case. We provided quantitative characterization of the solutions using modulation theory and qualitative identification of the PDSW solutions.

Second, the modulation equations exhibit nonconvexity where the modulation velocities coalesce. Adopting the method developed in [33], a nonclassical dispersive shock wave solution, a contact DSW (CDSW), is predicted when the system exhibits nonconvexity as a single wave or one component of a composite wave. A distinguishing feature is a short, smooth ramp at the algebraic soliton edge of a CDSW where the soliton connects to a dispersionless (nonoscillatory) portion of the solution.

While our analysis was developed for conservative spin dynamics applicable over short enough time scales, it has intriguing implications for longer times wherein magnetic damping leads to relaxation of the dynamics to a steady configuration. First, rarefaction waves expand in time with negligible oscillations. This implies that such a solution minimizes the excitation of spin waves in the system. On the contrary, spin shocks exhibit pronounced oscillations that can reflect many times in the channel before being quenched by magnetic damping. While this can be seen as a disadvantage, it is also important to note that the spin waves excited by a spin shock are launched within a specific spectral band that is determined by the transition between the left and right states [43], opening opportunities for controllable transport of angular momentum by means of pulsed injection. Such spin waves have typically high propagation speeds, recently observed in the context of current-induced domain wall motion in perpendicular magnetic anisotropic van der Waals magnets [14]. Second, we find that a stationary soliton established in the conservative regime can remain after stabilization via damping, resulting in the contact soliton-dissipative exchange flow [10]. Third, numerical simulations in [12] show that it is also possible to excite propagating soliton trains that persist, oscillating back and forth in the channel, even in the presence of damping. In additional simulations, we observe here that such solitons are excited precisely when the originating spin shock contains a CDSW. These are examples of situations where the transient dynamics impact the transport characteristics of the dissipative exchange flow in equilibrium.

The dispersive hydrodynamic interpretation of ferromagnetic dynamics allows one to adopt a large pool of analytical tools that are traditionally used for classical fluids, which provides new perspectives on the study and understanding of spin dynamics. The dynamical problem studied here has a problem setup that is designed to be experimentally accessible and we expect our methodology to aid the experimental realization of superfluid-like spin transport in the form of nonuniform magnetic textures.

ACKNOWLEDGMENTS

M.H. thanks T. Congy for the helpful discussions. All authors acknowledge support from the U.S. Department of Energy, Office of Science, Grant No. DE-SC0018237. M.A.H. acknowledges partial support from National Science Foundation DMS-1816934 and M.H. acknowledges support from the National Institute of Standards and Technology Professional Research Experience Program.

APPENDIX: DETERMINATION OF THE PHYSICAL WAVE PATTERN GIVEN RIEMANN INVARIANTS

In this Appendix, we present additional information on the characterization of periodic traveling wave solutions to the LL equation (1). The LL-Whitham equations in terms of the Riemann invariants $\lambda = (\lambda_1, \lambda_2, \lambda_3, \lambda_4)$ have been given in (23). The family of traveling waves dynamics satisfy Eq. (8). The quartic polynomial $R(n)$ can be written in terms of four roots $\{n_i\}_{i=1}^4$. It can also be expressed in terms of the Riemann invariants $\boldsymbol{\lambda}$ [33] where

$$R(n) = n^4 + \frac{s_1+s_3}{f_1}n^3 + s_2 n^2 + \left(f_1 s_1 - \frac{s_1+s_3}{f_1}\right)n + \frac{1}{4}\left(s_1^2 - 4 - 4s_2 + 4f_1^2\right), \tag{A1}$$

$$s_1 = \sum_i^4 \lambda_i,\ s_2 = \sum_{i<j}^4 \lambda_i\lambda_j,\ s_3 = \sum_{i<j<k}^4 \lambda_i\lambda_j\lambda_k,$$
$$s_4 = \lambda_1\lambda_2\lambda_3\lambda_4, \tag{A2}$$

$$\lambda_i' = \sqrt{1-\lambda_i^2}, \quad s_4' = \Pi_i^4 \lambda_i'. \tag{A3}$$

For a given set of Riemann invariants $\boldsymbol{\lambda}$, there are four possible physical wave patterns corresponding to four possible choices of f_1:

$$f_1 = \pm\sqrt{(1+s_2+s_4+s_4')/2}, \tag{A4a}$$

$$\text{or}\, f_1 = \pm\text{sgn}(s_1+s_3)\sqrt{(1+s_2+s_4-s_4')/2}, \tag{A4b}$$

This 4-valued mapping of Riemann invariants to traveling wave profiles implies that the LL-Whitham modulation system is nonconvex. Later, we denote f_{1a} as f_1 taking the positive expression in (A4a) and f_{1b} as f_1 taking the positive expression in (A4b). The fluid velocity can be computed from

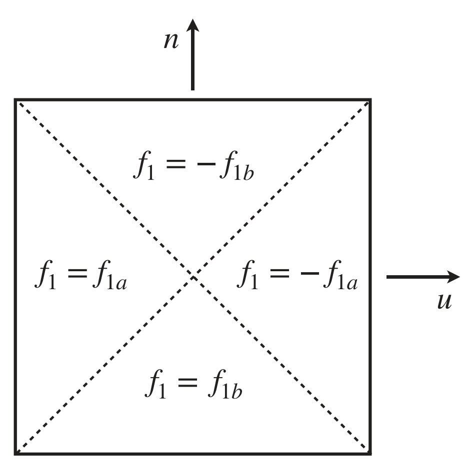

FIG. 11. The choice of f_1 depending on the location of (u^L, n^L).

the density as

$$u(\xi) = -\frac{f_1 + \frac{s_1}{2}n}{1 - n^2}. \tag{A5}$$

The multivalued mapping from the Riemann invariants to the roots of the potential function are [33]:

$$n_1 = -\frac{1}{2f_1}\frac{(\lambda_3-\lambda_2)\tilde{s}_1 + (\lambda_3-\lambda_1)\tilde{s}_2 - (\lambda_2-\lambda_1)\tilde{s}_3}{(\lambda_3-\lambda_2)\lambda_1' + (\lambda_3-\lambda_1)\lambda_2' - (\lambda_2-\lambda_1)\lambda_3'},$$

$$n_2 = -\frac{1}{2f_1}\frac{(\lambda_3-\lambda_2)\tilde{s}_1 + (\lambda_3-\lambda_1)\tilde{s}_2 + (\lambda_2-\lambda_1)\tilde{s}_3}{(\lambda_3-\lambda_2)\lambda_1' + (\lambda_3-\lambda_1)\lambda_2' + (\lambda_2-\lambda_1)\lambda_3'},$$

$$n_3 = -\frac{1}{2f_1}\frac{(\lambda_3-\lambda_2)\tilde{s}_1 - (\lambda_3-\lambda_1)\tilde{s}_2 - (\lambda_2-\lambda_1)\tilde{s}_3}{(\lambda_3-\lambda_2)\lambda_1' - (\lambda_3-\lambda_1)\lambda_2' - (\lambda_2-\lambda_1)\lambda_3'},$$

$$n_4 = -\frac{1}{2f_1}\frac{(\lambda_3-\lambda_2)\tilde{s}_1 - (\lambda_3-\lambda_1)\tilde{s}_2 + (\lambda_2-\lambda_1)\tilde{s}_3}{(\lambda_3-\lambda_2)\lambda_1' - (\lambda_3-\lambda_1)\lambda_2' + (\lambda_2-\lambda_1)\lambda_3'}, \tag{A6}$$

where $\tilde{s}_i = (s_1 - \lambda_i)\lambda_i' + s_4\frac{\lambda_i'}{\lambda_i} \mp s_4'\frac{\lambda_i}{\lambda_i'}$. The upper sign in $\tilde{s}_i$ is for f_{1a} given by (A4a) and the lower sign is for f_{1b} given by (A4b). The other two cases when $f_1 < 0$ leads to reordering of the expressions of n_i's, which is $n_i \leftarrow n_{5-i}$, $i = 1, 2, 3, 4$.

Depending on which triangle, divided by the diagonal and antidiagonal of the square $[-1, 1] \times [-1, 1]$ the left constant state (u^L, n^L) lies in, the choice of f_1 is shown in Fig. 11.

[1] E. Iacocca and M. A. Hoefer, Perspectives on spin hydrodynamics in ferromagnetic materials, Phys. Lett. A **383**, 125858 (2019).

[2] E. B. Sonin, Superfluid spin transport in magnetically ordered solids (Review article), Low Temp. Phys. **46**, 436 (2020).

[3] B. Halperin and P. Hohenberg, Hydrodynamic theory of spin waves, Phys. Rev. **188**, 898 (1969).

[4] J. König, M. C. Bønsager, and A. H. MacDonald, Dissipationless Spin Transport in Thin Film Ferromagnets, Phys. Rev. Lett. **87**, 187202 (2001).

[5] E. Sonin, Spin currents and spin superfluidity, Adv. Phys. **59**, 181 (2010).

[6] S. Takei and Y. Tserkovnyak, Superfluid Spin Transport Through Easy-Plane Ferromagnetic Insulators, Phys. Rev. Lett. **112**, 227201 (2014).

[7] H. Chen, A. D. Kent, A. H. MacDonald, and I. Sodemann, Nonlocal transport mediated by spin supercurrents, Phys. Rev. B **90**, 220401(R) (2014).

[8] E. Iacocca, T. J. Silva, and M. A. Hoefer, Breaking of Galilean Invariance in the Hydrodynamic Formulation of Ferromagnetic Thin Films, Phys. Rev. Lett. **118**, 017203 (2017).

[9] E. Iacocca, T. J. Silva, and M. A. Hoefer, Symmetry-broken dissipative exchange flows in thin-film ferromagnets with in-plane anisotropy, Phys. Rev. B **96**, 134434 (2017).

[10] E. Iacocca and M. A. Hoefer, Hydrodynamic description of long-distance spin transport through noncollinear magnetization states: Role of dispersion, nonlinearity, and damping, Phys. Rev. B **99**, 184402 (2019).

[11] M. Evers and U. Nowak, Transport properties of spin superfluids: Comparing easy-plane ferromagnets and antiferromagnets, Phys. Rev. B **101**, 184415 (2020).

[12] M. Hu, E. Iacocca, and M. A. Hoefer, Spin-injection-generated shock waves and solitons in a ferromagnetic thin film, IEEE Trans. Magn. **58**, 1300105 (2021).

[13] D. A. Smith, S. Takei, B. Brann, L. Compton, F. Ramos-Diaz, M. J. Simmers, and S. Emori, Diffusive and fluidlike motion of homochiral domain walls in easy-plane magnetic strips, Phys. Rev. Applied **16**, 054002 (2021).

[14] D. Abdul-Wahab, E. Iacocca, R. F. Evans, A. Bedoya-Pinto, S. Parkin, K. S. Novoselov, and E. J. Santos, Domain wall dynamics in two-dimensional van der Waals ferromagnets, Appl. Phys. Rev. **8**, 041411 (2021).

[15] P. Stepanov, S. Che, D. Shcherbakov, J. Yang, R. Chen, K. Thilahar, G. Voigt, M. W. Bockrath, D. Smirnov, K. Watanabe *et al.*, Long-distance spin transport through a graphene quantum Hall antiferromagnet, Nat. Phys. **14**, 907 (2018).

[16] T. Schneider, D. Hill, A. Kákay, K. Lenz, J. Lindner, J. Fassbender, P. Upadhyaya, Y. Liu, K. Wang, Y. Tserkovnyak, I. N. Krivorotov, and I. Barsukov, Self-stabilizing spin superfluid, Phys. Rev. B **103**, 144412 (2021).

[17] A. Hoffmann, Spin Hall effects in metals, IEEE Trans. Magn. **49**, 5172 (2013).

[18] W. Yuan, Q. Zhu, T. Su, Y. Yao, W. Xing, Y. Chen, Y. Ma, X. Lin, J. Shi, R. Shindou *et al.*, Experimental signatures of spin superfluid ground state in canted antiferromagnet Cr_2O_3 via nonlocal spin transport, Sci. Adv. **4**, eaat1098 (2018).

[19] G. El and M. Hoefer, Dispersive shock waves and modulation theory, Physica D **333**, 11 (2016).

[20] E. Iacocca and M. A. Hoefer, Vortex-antivortex proliferation from an obstacle in thin film ferromagnets, Phys. Rev. B **95**, 134409 (2017).

[21] E. Iacocca, Controllable vortex shedding from dissipative exchange flows in ferromagnetic channels, Phys. Rev. B **102**, 224403 (2020).

[22] P. A. P. Janantha, P. Sprenger, M. A. Hoefer, and M. Wu, Observation of Self-Cavitating Envelope Dispersive Shock Waves in Yttrium Iron Garnet Thin Films, Phys. Rev. Lett. **119**, 024101 (2017).

[23] M. A. Hoefer, M. J. Ablowitz, I. Coddington, E. A. Cornell, P. Engels, and V. Schweikhard, Dispersive and classical shock waves in Bose-Einstein condensates and gas dynamics, Phys. Rev. A **74**, 023623 (2006).

[24] T. Bienaimé, M. Isoard, Q. Fontaine, A. Bramati, A. M. Kamchatnov, Q. Glorieux, and N. Pavloff, Quantitative Analysis of Shock Wave Dynamics in a Fluid of Light, Phys. Rev. Lett. **126**, 183901 (2021).

[25] G. Xu, M. Conforti, A. Kudlinski, A. Mussot, and S. Trillo, Dispersive Dam-Break Flow of a Photon Fluid, Phys. Rev. Lett. **118**, 254101 (2017).

[26] S. Trillo, M. Klein, G. Clauss, and M. Onorato, Observation of dispersive shock waves developing from initial depressions in shallow water, Physica D **333**, 276 (2016).

[27] M. D. Maiden, N. K. Lowman, D. V. Anderson, M. E. Schubert, and M. A. Hoefer, Observation of Dispersive Shock Waves, Solitons, and Their Interactions in Viscous Fluid Conduits, Phys. Rev. Lett. **116**, 174501 (2016).
[28] H. W. Liepmann and A. Roshko, *Elements of Gasdynamics* (Wiley, New York, 1957).
[29] G. B. Whitham, Nonlinear dispersive waves, Proc. R. Soc. A. Math. Phys. Sci. **283**, 238 (1965).
[30] G. B. Whitham, *Linear and Nonlinear Waves*, Vol. 42 (John Wiley, New York, 2011).
[31] A. M. Kamchatnov, *Nonlinear Periodic Waves and Their Modulations: An Introductory Course* (World Scientific, Singapore, 2000).
[32] B. Riemann, über die fortpflanzung ebener luftwellen von endlicher schwingungsweite, Abh. d. Königl. Ges. d. Wiss. zu Göttingen **8**, 43 (1860).
[33] S. K. Ivanov, A. M. Kamchatnov, T. Congy, and N. Pavloff, Solution of the Riemann problem for polarization waves in a two-component Bose-Einstein condensate, Phys. Rev. E **96**, 062202 (2017).
[34] M. A. Hoefer, M. J. Ablowitz, and P. Engels, Piston Dispersive Shock Wave Problem, Phys. Rev. Lett. **100**, 084504 (2008).
[35] A. M. Kamchatnov and S. V. Korneev, Flow of a Bose-Einstein condensate in a quasi-one-dimensional channel under the action of a piston, J. Exp. Theor. Phys. **110**, 170 (2010).
[36] M. E. Mossman, M. A. Hoefer, K. Julien, P. G. Kevrekidis, and P. Engels, Dissipative shock waves generated by a quantum-mechanical piston, Nat. Commun. **9**, 4665 (2018).
[37] A. Bendahmane, G. Xu, M. Conforti, A. Kudlinski, A. Mussot, and S. Trillo, Phase transitions of photon fluid flows driven by a virtual all-optical piston, arXiv:2007.16060.
[38] G. El, M. Hoefer, and M. Shearer, Dispersive and diffusive-dispersive shock waves for nonconvex conservation laws, SIAM Rev. **59**, 3 (2017).
[39] P. F. Byrd and M. D. Friedman, *Handbook of Elliptic Integrals for Engineers and Physicists* (Springer-Verlag, Berlin, 1954).
[40] P. D. Lax, *Hyperbolic Systems of Conservation Laws and the Mathematical Theory of Shock Waves* (SIAM, Philadelphia, PA, 1973).
[41] R. Courant and K. O. Friedrichs, *Supersonic Flow and Shock Waves* (Springer-Verlag, Berlin, 1948).
[42] T. Marchant and N. Smyth, Initial-boundary value problems for the korteweg-de Vries equation, IMA J. Appl. Math. **47**, 247 (1991).
[43] M. Conforti, F. Baronio, and S. Trillo, Resonant radiation shed by dispersive shock waves, Phys. Rev. A **89**, 013807 (2014).